nature materials

Letter

https://doi.org/10.1038/s41563-023-01733-8

Oxidation-induced superelasticity in metallic glass nanotubes

Received: 18 April 2022

Accepted: 20 October 2023

Published online: 05 December 2023

Check for updates

Fucheng Li[1,2,3,10], Zhibo Zhang[1,10], Huanrong Liu[4,10], Wenqing Zhu[1], Tianyu Wang[1], Minhyuk Park[1], Jingyang Zhang[1], Niklas Bönninghoff[5], Xiaobin Feng[1], Hongti Zhang[1], Junhua Luan[6], Jianguo Wang[1], Xiaodi Liu[7], Tinghao Chang[5], Jinn P. Chu[5], Yang Lu[1,8], Yanhui Liu[2,3] ✉, Pengfei Guan[4] ✉ & Yong Yang[1,6,9] ✉

Although metallic nanostructures have been attracting tremendous research interest in nanoscience and nanotechnologies, it is known that environmental attacks, such as surface oxidation, can easily initiate cracking on the surface of metals, thus deteriorating their overall functional/structural properties[1–3]. In sharp contrast, here we report that severely oxidized metallic glass nanotubes can attain an ultrahigh recoverable elastic strain of up to ~14% at room temperature, which outperform bulk metallic glasses, metallic glass nanowires and many other superelastic metals hitherto reported. Through in situ experiments and atomistic simulations, we reveal that the physical mechanisms underpinning the observed superelasticity can be attributed to the formation of a percolating oxide network in metallic glass nanotubes, which not only restricts atomic-scale plastic events during loading but also leads to the recovery of elastic rigidity on unloading. Our discovery implies that oxidation in low-dimensional metallic glasses can result in unique properties for applications in nanodevices.

Low-dimensional metals, such as metallic films, nanosheets and nanowires, are promising candidate materials to construct three-dimensional (3D) micro- and nanodevices with tubular, spiral, reticular and architectural shapes owing to their distinct mechanical and functional properties[4–9], such as superelasticity[7–9]. However, unlike ceramics, most metals are electrochemically active and can easily react with oxygen to form surface native oxides when exposed to an ambient environment, which often causes the degradation of the physical properties of metals[1]. In principle, it is known that surface oxidation, which can induce the formation of undesirable interstitial impurities or oxides, can result in the embrittlement of metals, particularly for metallic nanomaterials with a high surface-to-volume ratio[2,3]. For example, the initiation of cracking in surface oxides can lead to a premature failure of nickel-based microdevices under cyclic loading[3]. Today, there is a pressing need to mitigate the negative influence of surface oxidation on metallic nanostructures, which is pivotal to the development of future nanodevices. In this Letter, however, we report an interesting finding demonstrating that surface oxidation becomes conducive to metallic glass (MG) nanotubes. Unlike crystalline metals, MGs are known for their lack of long-range periodic order and superior thermoplastic

[1]Department of Mechanical Engineering, College of Engineering, City University of Hong Kong, Kowloon Tong, Hong Kong, China. [2]Institute of Physics, Chinese Academy of Sciences, Beijing, China. [3]Songshan Lake Materials Laboratory, Dongguan, China. [4]Beijing Computational Science Research Center, Beijing, China. [5]Department of Material Science and Engineering, National Taiwan University of Science and Technology, Taipei, Taiwan. [6]Department of Materials Science and Engineering, College of Engineering, City University of Hong Kong, Kowloon Tong, Hong Kong, China. [7]College of Mechatronics and Control Engineering, Shenzhen University, Shenzhen, China. [8]Department of Mechanical Engineering, The University of Hong Kong, Pok Fu Lam, Hong Kong, China. [9]Department of System Engineering, College of Engineering, City University of Hong Kong, Kowloon Tong, Hong Kong, China. [10]These authors contributed equally: Fucheng Li, Zhibo Zhang, Huanrong Liu. ✉e-mail: yanhui.liu@iphy.ac.cn; pguan@csrc.ac.cn; yonyang@cityu.edu.hk

https://doi.org/10.1038/s41563-023-01733-8

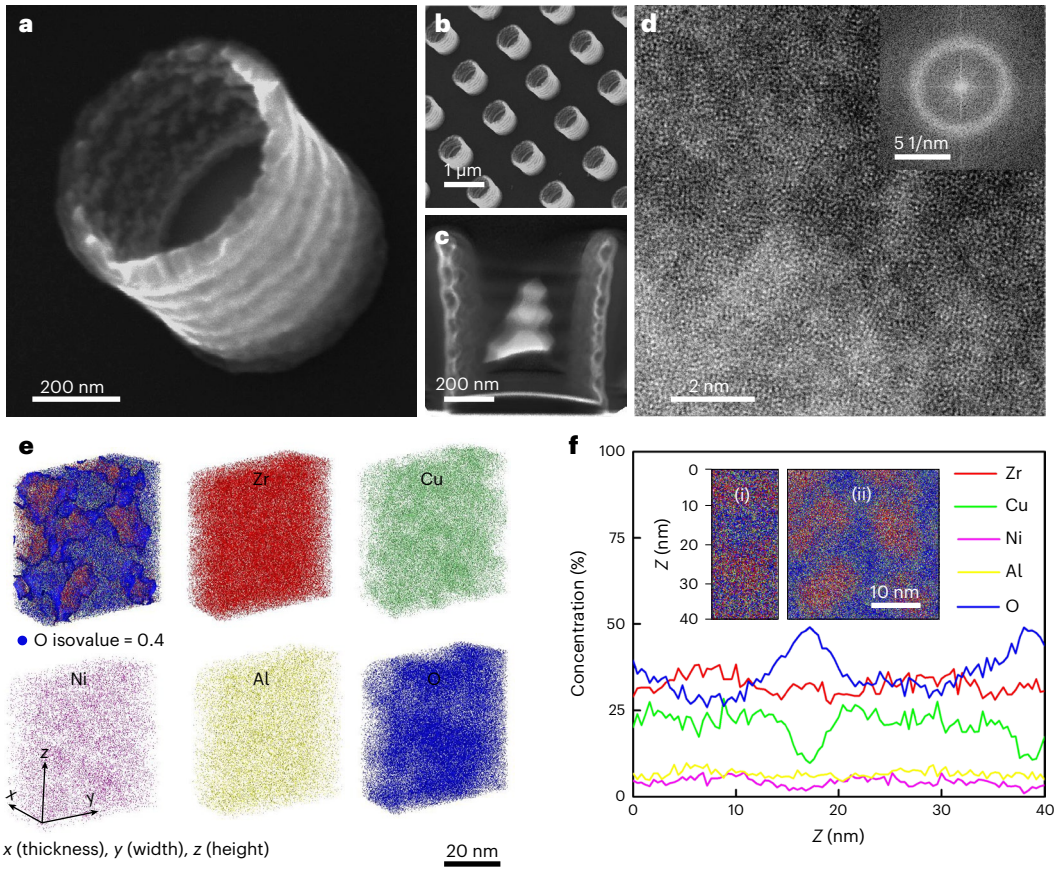

Fig. 1 | Structural and compositional characterizations of $Zr_{55}Cu_{30}Al_{10}Ni_5$ (at.%) MG nanotube. a, SEM image of a typical MG nanotube with the composition of $Zr_{55}Cu_{30}Al_{10}Ni_5$ (at.%). **b**, Array of MG nanotubes. **c**, Vertical sectional view of the MG nanotube. **d**, Amorphous structure of the MG nanotube characterized by spherical-aberration-corrected TEM (the inset shows the corresponding fast Fourier transform image). **e**, The 3D elemental distribution of a slice from the interior damage-free region of the nanotube obtained by 3D-APT. **f**, Elemental concentration of the $Zr_{55}Cu_{30}Al_{10}Ni_5$ (at.%) MG nanotube along the vertical sectional viewing direction inserted with the chemical distribution of atoms from different viewing angles (vertical sectional view (i) and side view (ii)).

formability[10,11]. Therefore, they are an excellent candidate material for micro- and nanodevices[8,12–14], such as superelastic nanolattices[8,14]. Very interestingly, here we show that oxygen can be easily dissolved in the amorphous structure of various MG nanotubes, which forms a network of metal–oxygen atomic clusters that leads to superelasticity, unmatched by that in bulk MGs (~2%) (ref. 15), MG nanowires (~5%) (refs. 16,17) and other superelastic metals (2–7%) (for example, high-entropy alloys[18], gum metals[19], shape memory alloys[20] and metal nanocomposites[21,22]).

Figure 1a,b shows an array of MG nanotubes with the chemical composition of $Zr_{55}Cu_{30}Al_{10}Ni_5$ (at.%) fabricated via the very-large-scale integration method[23]. The as-fabricated nanotubes are ~650 nm in height and ~500 nm in diameter, with a wall thickness ranging from ~15 to ~25 nm (average thickness, 20 nm). Interestingly, these nanotubes exhibit a wavy profile along their longitudinal direction with a wavelength of ~100 nm and amplitude of ~5 nm (Fig. 1c), which can be well fitted to a sinusoidal wavefunction (Extended Data Fig. 1). A similar wavy structure was observed in prior works[24,25] and attributed to a standing-wave effect in photoresists[25]. With finite-element method (FEM) simulations (Methods), we demonstrate that this wavy tubular structure is mechanically robust against buckling in comparison with straight-walled hollow tubes, as discussed later. Furthermore, we characterized the atomic structure of the MG nanotubes by spherical-aberration-corrected transmission electron microscopy (TEM), which shows that the nanotubes are fully amorphous (Fig. 1d), consistent with prior results[23,24].

Given the ultrahigh surface-to-volume ratio (~10^8 m^{-1}), our MG nanotubes are susceptible to surface oxidation. We performed three-dimensional atom probe tomography (3D-APT) analyses (Methods), which show a 3D elemental distribution (Fig. 1e) of a slice from the interior damage-free region of the nanotube. As shown in Fig. 1e, there is a clear segregation of elemental O from the MG matrix, forming a percolating network structure as we use the O-concentration isovalue of 0.40 as a threshold, which was greater than the average concentration of O (~0.37) to define the oxide-rich regions. We also provide APT analyses from different viewing angles to fully understand the percolating network of oxygen-rich regions (Fig. 1f). From a typical side view (Fig. 1f(ii) and illustrated in Extended Data Fig. 2a), nanosized metal-rich regions surrounded by interconnected oxide-rich regions can be clearly observed (Fig. 1f). On the other hand, a columnar-like or sandwich-like structure is evident from the vertical sectional view (Fig. 1f(i) and illustrated in Extended Data Fig. 2a), suggesting that the topology of the interconnected oxide-rich regions should be close to two dimensions (Fig. 1f). Furthermore, the chemical distribution along the vertical sectional direction reveals that the oxygen concentration can reach ~50% in the centre of the oxygen-rich regions but gradually reduces to 25% in their peripheries (Fig. 1f). A similar phenomenon can also be observed in the electron energy loss spectroscopy (EELS) result on our MG nanotubes (Extended Data Fig. 2b,c) and freestanding 20-nm-thick $Zr_{55}Cu_{30}Al_{10}Ni_5$ (at.%) nanosheets peeling off from the photoresist substrate (Methods and Supplementary Fig. 1a–d). In addition, via X-ray photoelectron spectroscopy, we carried out depth

https://doi.org/10.1038/s41563-023-01733-8

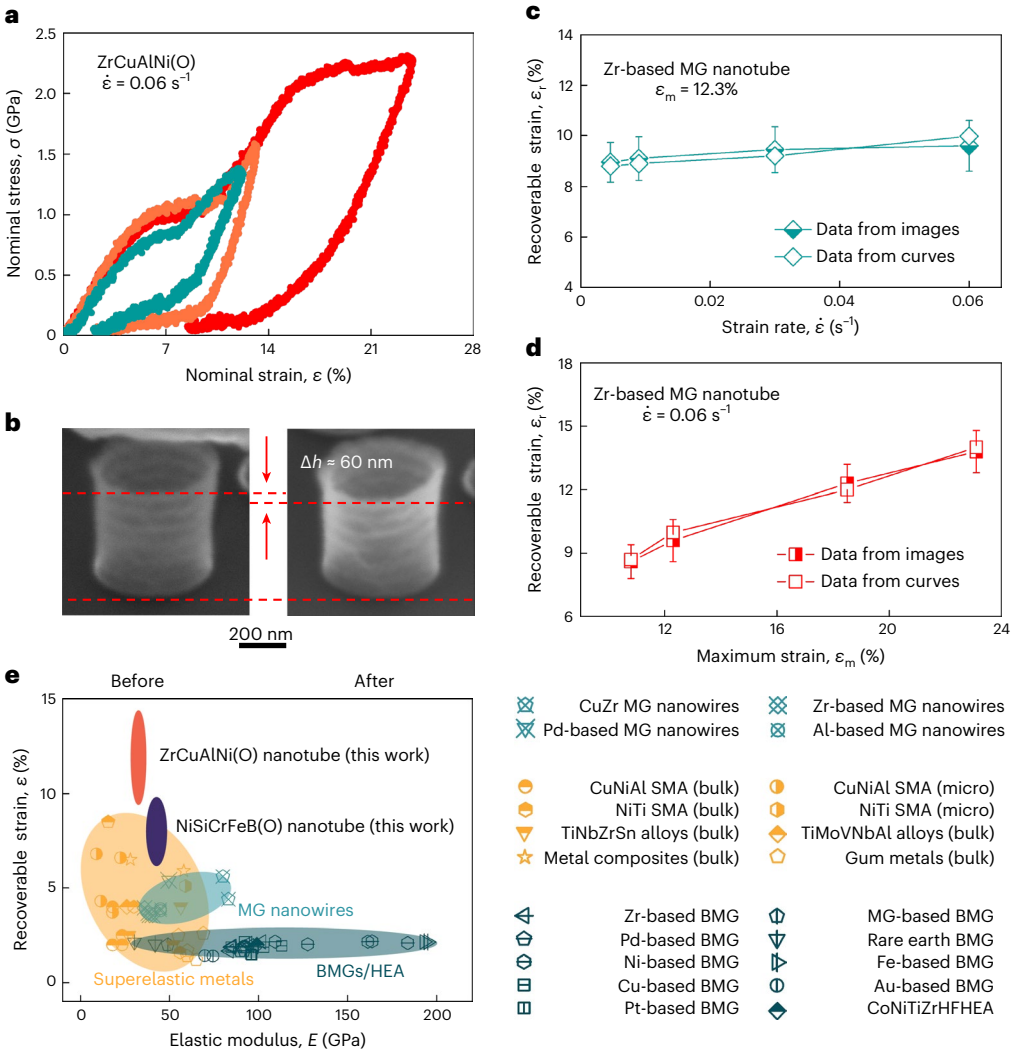

Fig. 2 | Mechanical behaviour of the $Zr_{55}Cu_{30}Al_{10}Ni_5$ (at.%) MG nanotubes. **a**, Nominal stress–strain curves of the ZrCuAlNi(O) MG nanotubes with an average wall thickness of ~20 nm. **b**, ZrCuAlNi(O) MG nanotube before and after microcompression to the maximum strain of 23.1%. **c**, Effect of the strain rate on the recoverable strain, measured from either stress–strain curves or image correlations, for the ZrCuAlNi(O) MG nanotubes. Note that the recoverable strains measured from image correlations were repeated five times for averaging and data are presented as mean values ± standard deviation (s.d.). **d**, Effect of maximum strain on the measured recoverable strain for the ZrCuAlNi(O) MG nanotubes. Note that the recoverable strains measured from image correlations were repeated five times for averaging and data are presented as mean values ± s.d. **e**, Comparison of the recoverable strain versus elastic modulus of various superelastic metals. (BMG = bulk metallic glass, HEA = high entropy alloy, SMA = shape memory alloy).

profiling on the 20-nm-thick nanosheets (Methods), and identified that the oxides are mainly ZrO_2 and Al_2O_3, whereas the amorphous metals comprise Zr, Cu, Ni and Al (Supplementary Fig. 1e).

Figure 2a shows three nominal compressive stress–strain curves obtained from the $Zr_{55}Cu_{30}Al_{10}Ni_5$ MG nanotube at a strain rate of 0.06 s^{-1}. We note that the nanotubes were pressed to a maximum strain of 10.8%, 12.3% and 23.1% and yielding seemingly occurred at the inflection points on the stress–strain curves. Interestingly, we observed a remarkable recovery of deformation on the removal of the external load, which shows 8.7%, 10.0% and 14.1% strain recovery for these three respective tests. To further validate these findings, we measured the heights of the MG nanotubes via in situ microcompression experiments (Supplementary Video 1), as shown in Fig. 2b for the nanotube pressed to a 23.1% strain. Similar findings were observed on the $Ni_{38}Si_{53}Cr_6Fe_2B_1$ MG nanotubes (Extended Data Fig. 3a), which showed ~9.1% recoverable strain after a maximum strain of 15.4% (Extended Data Fig. 3a,b). Similarly, we also validated the large recoverable strain in the Ni-based MG nanotubes by multiple instances of in situ testing (Supplementary Video 2) and image correlation (Extended Data Fig. 3d). Furthermore, we systematically investigated the effects of strain rate and maximum strain on the strain recovery in our nanotubes. As shown in Fig. 2c,d for ZrCuAlNi(O), it is interesting to note that although the recoverable strain increases with the applied maximum strain, they are insensitive to the strain rate, which indicates that the recoverable strain is not due to anelasticity in MGs[26]. A similar result was obtained for the NiSiCrFeB(O) MG nanotubes (Extended Data Fig. 3c).

Next, we carried out extensive FEM simulations (Methods) to investigate the geometric effect of the nanotubes on their deformation behaviour. In particular, we observed that neither wavy nor regular cross-sectional tubular structures exhibited remarkable strain recovery (Extended Data Fig. 4a,b and Supplementary Fig. 5) when using the constitutive relation of either the Drucker–Prager model[27] or the free-volume model[28] in our FEM simulations, even considering the possible size effect due to the fast surface atom mobility of MGs. Besides, we note that no sudden stress drop can be observed on the stress–strain curves of our nanotubes, which delivers a strong message that elastic

https://doi.org/10.1038/s41563-023-01733-8

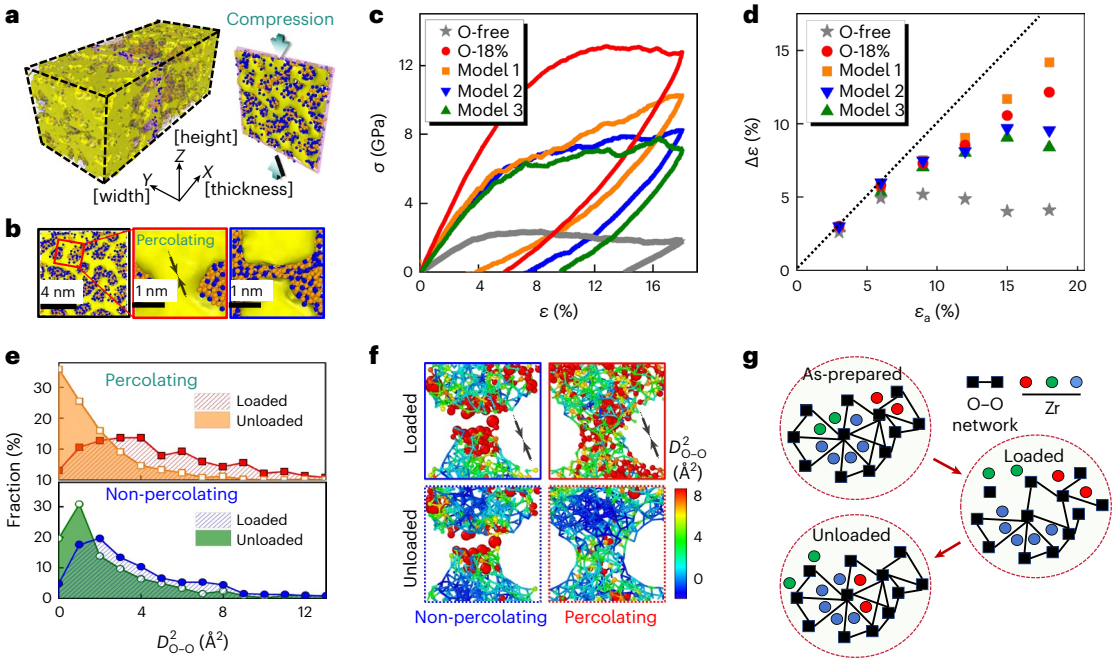

Fig. 3 | Atomic origin of superelasticity in Cu–Zr(O) MGs. a, A 3D view and profile of the oxide network and metal-rich region. The uniaxial compression is applied along the *Z* axis. **b**, Zoomed-in view of the local morphologies of percolating (red box) and non-percolating (blue box) oxide networks. The oxide region is visualized by smooth surface meshes (yellow) and Cu/Zr atoms are shown as orange/blue balls. The load direction is labelled with black arrows. **c**, Typical stress–strain curves of various MG samples with a distinct oxide network under mechanical loading–unloading with a compressive strain amplitude of up to 18%. **d**, Recoverable strain ($\Delta\varepsilon$) as a function of loading strain amplitude (ε_a). **e**, Fraction distributions of calculated non-affine displacement (D^2_{O-O}) of the oxide network in loaded samples under $\varepsilon_a = 0.18$ and strain-free unloaded samples. **f**, Snapshots of the oxide network in loaded and unloaded samples. Only O atoms are shown, and their colour and radius are given by the calculated D^2_{O-O}. **g**, Illustrated atomic-scale bond-switching mechanism underlying the self-healing phenomenon of the O network with the undirected graph-mapping method (black squares and bonds, O atoms and O–O network, respectively; red spheres, bonding Zr atoms; green spheres, break-bonding Zr atoms; blue spheres, stable Zr atoms).

buckling is not incurred[8] and the large recoverable strain (14%) in our nanotubes is an intrinsic property (Fig. 2a). This is fundamentally different from the superelastic behaviour observed in metallic nanolattices, the latter of which originates from a collective mechanical behaviour of their tubular ligaments after elastic buckling[8,9]. We also studied the effect of load misalignment in the FEM simulations by varying the angle of the loading axis with the central line of the tube from 0° to 10°. Again, we did not find any pronounced effect of load misalignment on the deformation recovery in the tubes. To further explore the origin of superelasticity, we prepared freestanding 20-nm-thick $Zr_{55}Cu_{30}Al_{10}Ni_5$ (at.%) nanosheets by physical vapour deposition and subsequent exfoliation from the NaCl, polyvinyl alcohol (PVA) and photoresist substrates, the last of which followed a similar fabrication method as our nanotubes (Methods). According to our results from the TEM and electrically conductive atomic force microscopy (AFM) (Methods), the MG nanosheets from the PVA and photoresist have been oxidized to a much higher degree than those from the NaCl substrate (Supplementary Fig. 2a,d,g), which could be attributed to the reaction between metals and polymers as discussed elsewhere[29]. Interestingly, the thinner (for example, more oxidized) nanosheets appear to be more superelastic than the thicker (for example, less oxidized) ones under AFM indentation (Methods and Supplementary Figs. 3 and 4). We performed a systematic study of this thickness effect using the nanosheets oxidized to different degrees. According to our AFM experiments (that is, conductive AFM and indentation), we found that the thicker nanosheets (thickness, ≳30 nm) contained fewer oxides, as indicated by the insulating areas appearing as isolated 'patches' (Supplementary Fig. 3), and their superelasticity is almost thickness independent (Methods and Supplementary Fig. 4). In contrast, the thinner nanosheets were severely oxidized, which show thickness-dependent oxidation and superelasticity (Supplementary Figs. 3a–f and 4). Based on the above analyses, we conclude that the remarkable strain recovery we observed in the nanotubes must have a physical origin related to nanoscale oxidation.

Through the FEM simulations, we can extract the elastic modulus of the MG nanotubes through data fitting (Methods). As shown in the Extended Data Fig. 5a,b, we estimate that the elastic modulus of the Zr-based MG nanotube should range from 20 to 37 GPa with an average value of 29 ± 9 GPa for the wave-like structures observed in Extended Data Fig. 6a–c, which is consistent with our FEM simulation results on our ~20-nm-thick nanosheets with an elastic modulus of ~40 GPa (Supplementary Fig. 2c,f,i). Similarly, we estimate that the elastic modulus of the Ni-based MG nanotubes should range from 27 to 52 GPa (Extended Data Fig. 5a,b) with an average value of 40 ± 13 GPa. Figure 2e compares the recoverable strains of both Zr- and Ni-based MG nanotubes with those of the reported superelastic metals in the literature, including bulk MGs, MG nanowires, high-entropy alloys and some others (Supplementary Table 1). Evidently, our MG nanotubes are soft and elastically resilient, which outperform other superelastic metals hitherto reported in terms of their ultrahigh recoverable strains despite the difference in size and geometry between these nanotubes and other metals.

To understand the atomic origin of superelasticity in our MG nanotubes, we performed extensive molecular dynamics (MD) simulations based on the neural network interatomic potential (Methods) that considers the bonding of oxygen with metallic elements (for example, Cu, Zr). To this end, we first prepared the Cu–Zr–O model glass with an average O concentration ($\bar{C_O}$) of 0.18 (denoted as O-18%; Methods). To mimic the experiments, an O-concentration gradient (Extended Data Fig. 7a) was also introduced into the model. As a result,

the O-rich regions percolate to form a percolating network structure after structural relaxation (Fig. 3a,b), which generally agrees with our experimental results, such as the data from 3D-APT (Fig. 1e), EELS elemental mapping (Extended Data Fig. 2 and Supplementary Fig. 1d) and electrically conductive AFM mapping (Supplementary Fig. 2a,d,g). The dimension of the percolating network was fitted to be ~2.3 using the box-counting method (Methods). For the sake of comparison, we also prepared various model glasses without O (with $\bar{C_O} = 0$, denoted as O-free), and with percolating (Extended Data Fig. 7b,c, denoted as models 1 and 2, respectively) and non-percolating (Extended Data Fig. 7d, denoted as model 3) oxide networks with $\bar{C_O} \approx 18\%$.

Figure 3c compares the loading–unloading stress–strain curves obtained from five types of MG model glass (that is, models 1, 2 and 3 with different dimensions of oxide networks, as prepared using O-free and O-18% samples). It is evident that the amorphous structures with a percolating oxide network are much more elastically resilient, exhibiting a recoverable strain ($\Delta\varepsilon$) of ~14.0% when subjected to a maximum strain ε of 18.0%, which contrasts the recoverable strain of only ~8.5% and ~4.0% obtained for the non-percolating oxides and O-free MG model glasses, respectively. Furthermore, we studied the effect of ε on $\Delta\varepsilon$. As shown in Fig. 3d, $\Delta\varepsilon$ increases with ε for the O-containing model glasses before ε reaches 15%, after which $\Delta\varepsilon$ continues to rise for the model with percolating oxides whereas drops for the model with non-percolating oxides. By comparison, $\Delta\varepsilon$ remains more or less a constant for the O-free model glass.

To further identify the structural origin underpinning the remarkable superelasticity, the non-affine squared displacements (D^2) were calculated (Methods) in both loaded and unloaded model glasses with and without the percolating oxides. The calculated values of D^2 in the Zr–Cu MG regions are presented in Extended Data Fig. 8, which show that more than 70% of large non-affine deformations ($D^2 \geq 7.5$ Å^2) are attributed to the regular local shear transformation in the MG region and cannot be recovered. Figure 3e shows the statistical distributions of the non-affine displacements D^2_{O-O} calculated for the O atoms. Clearly, a relatively large fraction (20–34%) of the non-affine displacement D^2_{O-O} is recovered on unloading, particularly when the oxides percolate. Figure 3f displays the snapshots of severely deformed regions in our model glass during loading and after unloading. It is noteworthy that with the aid of the percolation network, substantial atomic rebonding takes place on stress removal, even in the regions where atomic debonding occurs during loading. Through these atomic-scale rebonding processes, local reconnections are built, giving rise to an overall structural integrity and hence strain recovery. More interestingly, we note that the reconnections may be built at the atomic sites different from those disrupted during loading. In other words, the percolating oxide network is polymorphic, which is analogous to the damage-tolerant networks discussed elsewhere[30,31]. Figure 3g shows a local view of such a disconnection-and-reconnection process. Clearly, debonding occurs between the Zr–O atomic pairs, resulting in the disruption of the network, which do not rebond after unloading; instead, bonding takes place in the neighbourhood of the debonding site, thereby restoring the connections that result in the elastic rigidity of the O–O network. In our MD simulations, we found that these bond-switching processes are abundant in the interfacial region between the oxides network and Zr–Cu MG regions but relatively few elsewhere (Fig. 3f). In light of these findings, we conclude that oxidation in our MG nanotubes facilitates superelasticity.

In summary, we experimentally demonstrate that MG nanotubes are superelastic at room temperature, which outperform various superelastic metals and alloys known to date. According to our atomistic simulations, this superelasticity originates from severe oxidation in the nanotubes and can be attributed to the formation of a damage-tolerant percolation network of nano-oxides in the amorphous structure. This unique property of the MG nanostructures is useful, which could find many applications in future nanodevices working in harsh environments, such as sensors, medical devices, micro- or nanorobots, springs and actuators[6,7,12,32].

Online content

Any methods, additional references, Nature Portfolio reporting summaries, source data, extended data, supplementary information, acknowledgements, peer review information; details of author contributions and competing interests; and statements of data and code availability are available at https://doi.org/10.1038/s41563-023-01733-8.

References

1. Cabrera, N. & Mott, N. F. Theory of the oxidation of metals. *Rep. Prog. Phys.* **12**, 163–184 (1949).
2. Boyce, B. L., Michael, J. R. & Kotula, P. G. Fatigue of metallic microdevices and the role of fatigue-induced surface oxides. *Acta Mater.* **52**, 1609–1619 (2004).
3. Barrios, A., Gupta, S., Castelluccio, G. M. & Pierron, O. N. Quantitative in situ SEM high cycle fatigue: the critical role of oxygen on nanoscale-void-controlled nucleation and propagation of small cracks in Ni microbeams. *Nano Lett.* **18**, 2595–2602 (2018).
4. Chen, Y. et al. Two-dimensional metal nanomaterials: synthesis, properties, and applications. *Chem. Rev.* **118**, 6409–6455 (2018).
5. Ruck, M. At the edge of covalency: metallic nanotubes, low-dimensional metals and clusters. *Z. Kristallogr. Cryst. Mater.* **225**, 167–172 (2010).
6. Wang, T., Park, M., Yu, Q., Zhang, J. & Yang, Y. Stability and synthesis of 2D metals and alloys: a review. *Mater. Today Adv.* **8**, 100092 (2020).
7. Schaedler, T. A. et al. Ultralight metallic microlattices. *Science* **334**, 962–965 (2011).
8. Lee, S.-W., Jafary-Zadeh, M., Chen, D. Z., Zhang, Y.-W. & Greer, J. R. Size effect suppresses brittle failure in hollow $Cu_{60}Zr_{40}$ metallic glass nanolattices deformed at cryogenic temperatures. *Nano Lett.* **15**, 5673–5681 (2015).
9. Maloney, K. J. et al. Microlattices as architected thin films: analysis of mechanical properties and high strain elastic recovery. *APL Mater.* **1**, 022106 (2013).
10. Schroers, J. Processing of bulk metallic glass. *Adv. Mater.* **22**, 1566–1597 (2010).
11. Duan, G. et al. Bulk metallic glass with benchmark thermoplastic processability. *Adv. Mater.* **19**, 4272 (2007).
12. Kumar, G., Tang, H. X. & Schroers, J. Nanomoulding with amorphous metals. *Nature* **457**, 868–872 (2009).
13. Li, J., Doubek, G., McMillon-Brown, L. & Taylor, A. D. Recent advances in metallic glass nanostructures: synthesis strategies and electrocatalytic applications. *Adv. Mater.* **31**, 1802120 (2019).
14. Jang, D., Meza, L. R., Greer, F. & Greer, J. R. Fabrication and deformation of three-dimensional hollow ceramic nanostructures. *Nat. Mater.* **12**, 893–898 (2013).
15. Johnson, W. L. & Samwer, K. A universal criterion for plastic yielding of metallic glasses with a $(T/T_g)^{2/3}$ temperature dependence. *Phys. Rev. Lett.* **95**, 195501 (2005).
16. Tian, L. et al. Approaching the ideal elastic limit of metallic glasses. *Nat. Commun.* **3**, 609 (2012).
17. Jiang, Q. K. et al. The effect of size on the elastic strain limit in $Ni_{60}Nb_{40}$ glassy films. *Acta Mater.* **61**, 4689–4695 (2013).
18. He, Q. F. et al. A highly distorted ultraelastic chemically complex Elinvar alloy. *Nature* **602**, 251–257 (2022).
19. Saito, T. et al. Multifunctional alloys obtained via a dislocation-free plastic deformation mechanism. *Science* **300**, 464–467 (2003).
20. Juan, J. S., Nó, M. L. & Schuh, C. A. Nanoscale shape-memory alloys for ultrahigh mechanical damping. *Nat. Nanotechnol.* **4**, 415–419 (2009).

21. Zhang, J. et al. Achieving 5.9% elastic strain in kilograms of metallic glasses: nanoscopic strain engineering goes macro. *Mater. Today* **37**, 18–26 (2020).
22. Hao, S. et al. A transforming metal nanocomposite with large elastic strain, low modulus, and high strength. *Science* **339**, 1191–1194 (2013).
23. Chen, J.-K., Chen, W.-T., Cheng, C.-C., Yu, C.-C. & Chu, J. P. Metallic glass nanotube arrays: preparation and surface characterizations. *Mater. Today* **21**, 178–185 (2018).
24. Chen, W.-T., Li, S.-S., Chu, J. P., Feng, K. C. & Chen, J.-K. Fabrication of ordered metallic glass nanotube arrays for label-free biosensing with diffractive reflectance. *Biosens. Bioelectron.* **102**, 129–135 (2018).
25. Wang, C., Jones, R. L., Lin, E. K., Wu, W.-L. & Leu, J. Small angle X-ray scattering measurements of lithographic patterns with sidewall roughness from vertical standing waves. *Appl. Phys. Lett.* **90**, 193122 (2007).
26. Ye, J. C., Lu, J., Liu, C. T., Wang, Q. & Yang, Y. Atomistic free-volume zones and inelastic deformation of metallic glasses. *Nat. Mater.* **9**, 619–623 (2010).
27. Zhao, M. & Li, M. Comparative study of elastoplastic constitutive models for deformation of metallic glasses. *Metals* **2**, 488–507 (2012).
28. Gao, Y. F., Yang, B. & Nieh, T. G. Thermomechanical instability analysis of inhomogeneous deformation in amorphous alloys. *Acta Mater.* **55**, 2319–2327 (2007).
29. Zhang, J. et al. Strong yet ductile high entropy alloy derived nanostructured cermet. *Nano Lett.* **22**, 7370–7377 (2022).
30. Albert, R., Jeong, H. & Barabási, A.-L. Error and attack tolerance of complex networks. *Nature* **406**, 378–382 (2000).
31. Sajadi, S. M. et al. Damage-tolerant 3D-printed ceramics via conformal coating. *Sci. Adv.* **7**, eabc5028 (2021).
32. Matovic, J. & Jakšić, Z. Nanomebrane: a new MEMS/NEMS building block. in *Micro Electronic and Mechanical Systems* 61–84 (Books on Demand, 2009).

Methods

Sample preparation

The $Zr_{55}Cu_{30}Al_{10}Ni_5$ (at.%) and $Ni_{38}Si_{53}Cr_6Fe_2B_1$ (at.%) MG nanotubes were prepared by using a very-large-scale integration method[24]. First, single-crystal Si wafers, Si(001), were cleaned by ultrasound, organic solvents (acetone, methanol and chloroform) and 50 wt% HF solution to remove surface contaminants followed by the surface oxidation of Si with a mixture of H_2SO_4 and H_2O_2 (2:1 mol%) and double-distilled water. Second, the Si wafers were treated by hexamethyldisilazane and placed with a positive photoresist (~780 nm) followed by I-line irradiation under masks of hole arrays and dissolving the exposed regions by the developer. Third, contact hole arrays with a certain diameter were successively generated on the photoresist after hard baking at 120 °C. Last, the as-prepared photoresist substrates were used to coat both $Zr_{55}Cu_{30}Al_{10}Ni_5$ (at.%) and $Ni_{38}Si_{53}Cr_6Fe_2B_1$ (at.%) MG coatings through radio-frequency magnetic sputtering systems with base and working pressures of ~5×10^{-4} and 3 mtorr, respectively, after which the residual photoresist was removed from the silicon surface by dipping with toluene to leave the MG nanotube arrays on the surface.

The freestanding ZrCuAlNi MG nanosheets were fabricated using an approach similar to the nanotubes[33]. To begin with, we spin coated a photoresist layer onto a hexamethyldisilazane-treated Si wafer. Subsequently, the ZrCuAlNi MG was deposited via physical vapour deposition at ~5×10^{-4} Pa base pressure and ~3 mtorr working pressure on the as-prepared photoresist substrate with thickness similar to our nanotubes (Supplementary Fig. 2i). Afterwards, the MG–photoresist–Si wafer system was immersed into acetone to remove the photoresist, which results in the delamination of the nanosheets. For comparison, we deposited the ZrCuAlNi MG film in a similar fashion via physical vapour deposition on both NaCl and PVA substrates and dissolved the NaCl and PVA substrates in deionized water to obtain the freestanding nanosheets.

Structural and compositional characterizations

The structural features of the $Zr_{55}Cu_{30}Al_{10}Ni_5$ (at.%) MG nanotube were first characterized by scanning electron microscopy (SEM) (FEI Quanta FEG450). Then, the morphology, atomic structure and EELS mapping of the MG nanotubes were observed on a JEM-ARM200F spherical-aberration-corrected TEM equipment. The 3D-APT characterization was performed in a local electrode atom probe (CAMEACA LEAP 5000 XR) instrument at 70 K in the voltage mode with a pulse repetition rate of 200 kHz, pulse fraction of 20% and evaporation detection rate of 0.1% atom per pulse. Reconstruction and visualization of the APT data were performed using the data analysis workstation AP Suite 6.1. Both TEM and needle-shaped 3D-APT specimens of $Zr_{55}Cu_{30}Al_{10}Ni_5$ (at.%) nanotube were prepared on an FEI SEM/focused-ion-beam system following annular milling and lift-out procedures.

The thickness of the prepared ZrCuAlNi nanosheets was measured by AFM (MFP-3D Infinity, Oxford Instruments) using a diamond-like carbon tip. The morphology and atomic structure of the nanosheets were characterized by SEM (FEI Quanta FEG450) and TEM (JEOL 2100F) and the EELS mapping of the MG nanosheets was obtained by a JEM-ARM200F spherical-aberration-corrected TEM equipment at 200 kV. The chemical states of all the elements (Zr, Cu, Al, Ni and O) were determined by X-ray photoelectron spectroscopy (Thermo Fisher, Nexsa) using monochromatic Al Kα radiation (12 kV, 6 mA) with an excitation energy of 1,486.68 eV. The depth profile analysis was performed by using an Ar-ion beam to etch the nanosheets at 2,000 eV with a spot size of 2×4 mm^2.

Mechanical and electrical conductive AFM characterizations

In situ microcompression tests of MG nanotubes were carried out on a quantitative piconindenter (PI85, Hysitron) system equipped with diamond conical flat punch tips (2 μm, Synton-MDP) inside the SEM instrument (FEI Quanta FEG450) by pushing the MG nanotubes against the diamond indenter in a step-by-step displacement control mode at different loading rates of 3, 6, 20 and 40 nm s^{-1}. Load and displacement were recorded in real time for different maximum displacements, ranging from 70 to 150 nm for the ZrCuNiAl MG nanotubes and from 50 to 100 nm for the NiSiCrFeB MG nanotubes.

The mechanical behaviour of freestanding nanosheets was investigated by using AFM indentation according to previous work[29,34]. First, the freestanding nanosheets were transferred to a Si wafer with holes. Afterwards, we characterized the topography of the suspended nanosheets by AFM and moved the tip to the centre of the hole. The force–displacement curves were extracted by indenting the suspended nanosheets using AFM with a diamond-like carbon tip of a tip radius of ~20 nm (Supplementary Fig. 2b,e,h). Sequential loading–unloading AFM indentation with a force increment of 100 nN was carried out under displacement control with the extend and retract velocity of 300 nm s^{-1}.

The electrical conductivity of the nanosheets was studied by conductive AFM. Doped diamond-coated silicon tips with a radius of ~20 nm were used to measure the point-wise electric current. To avoid the anodic oxidation of the nanosheets, we applied a negative voltage on the sample surface, leading to an electric current with a negative sign. To eliminate the effects of possible surface contamination, the surface materials of the nanosheets were removed by initial AFM scanning until the electric current became stable. To avoid exceeding the limit of the measurable electric current (±20 nA), we applied a voltage of −0.1 V on the nanosheets peeling off from NaCl, −1.0 V on the nanosheets from photoresist and −3.5 V on the nanosheets from PVA.

Image correlation

The nanoscale displacement and strain were measured with the digital image correlation method using the VIC-2D commercial software (Correlated Solutions). First, we converted the in situ compression video into a series of images and marked the unreformed one as the reference image. The tracking areas included ~25–50 pixels and were fixed at the top and bottom of the nanotube, along the compression direction. A normalized squared differences method was selected in the subsequent image correlation.

FEM simulation

Using ANSYS, we built several 3D structures based on the geometry and size of the nanotubes, with their height fixed at 650 nm, diameter at 500 nm, wall thickness ranging from 15 to 25 nm, wavelength from 80 to 105 nm and wave amplitude from 0 to 10 nm. A ten-node tetrahedral structural solid element 187 and the pressure sensitive Drucker–Prager model[27] were used in the meshing of the numerical models.

We also simulated the deformation behaviour of the MG nanotube using the classical free-volume model[28], which was implemented in an open-source FEM code, FEniCS. The height, diameter and thickness of the 3D nanotube model are 650, 500 and 20 nm, respectively. A first-order Lagrange element was used with a mesh size of approximately 4 nm. The initial conditions of the nanotube model with a phase-separated oxygen distribution was obtained by the Cahn–Hilliard approach[35].

The elastic modulus of the nanosheets was extracted from FEM through ANSYS following previous works[29,34]. An axisymmetric sector model was built as the suspended nanosheets, whereas the thickness, radius and sagging depth of the model were determined from the actual topography of the nanosheets. For simplicity, the Poisson's ratio of the nanosheets was assumed to be 0.33. To extract their elastic modulus, a linear-elastic model was employed in FEM. Meanwhile, the diamond-like carbon tip was modelled as a rigid sphere of a 20 nm radius with a frictionless contact. By fitting the elastic portion of the AFM force–displacement curves to FEM (Supplementary Fig. 2c,f,i), we can extrapolate the elastic modulus of the nanosheets as well as obtain the recoverable strain as the maximum von Mises stress that can be keyed to the recoverable experimental load.

Atomistic simulations

Zr–Cu–O neural network potentials. Accurate Zr–Cu–O neural network potentials were trained by our implementation with a new structure descriptor based on the self-developed spherical Chebyshev basis[36], which is more suitable for multicomponent MG systems. Supplementary Note 3 provides more details about the training process.

Preparation of Cu–Zr(O) model glassy samples. Five kinds of sample were prepared by performing MD simulations using LAMMPS[37] based on our developed Zr–Cu–O neural network potential. The O-free system with a size of 19.2 × 9.6 × 9.6 nm^3 was first equilibrated at 2,000 K and then quenched from 1,500 to 300 K at a rate of 10^{12} K s^{-1} using an isothermal–isobaric ensemble sampling (proposed in another work[38]) with zero external pressure.

For the O-18% sample, we randomly inserted interstitial oxygen atoms (C_O = 18.0%) in the Voronoi vertices of O-free Zr–Cu samples with a modulated gradient of O concentration (Extended Data Fig. 7a). The O-18% sample was equilibrated at 1,500 K for 1 ns and then quenched from 1,500 to 300 K at a rate of 10^{12} K s^{-1}. The percolating (model 1; Extended Data Fig. 7b) configuration was extracted from a profile of the O-18% sample with the same oxygen concentration in a small volume (3.2 × 3.2 × 3.2 nm^3). The under-percolating (model 2; Extended Data Fig. 7c) and non-percolating (model 3; Extended Data Fig. 7d) counterparts were prepared by replacing some O atoms with Cu atoms within a 'bottleneck' layer (width, 1 Å) in two-dimensional percolating configurations and optimized afterwards through structural relaxation. The replaced atoms only account for 0.5% of the total in the final configuration, which does not affect the pair correlation, signalling an amorphous structure (Extended Data Fig. 9). The oxide network was constructed by the '–O–Zr–O–' unit and a 3.0 Å cutoff was applied to select the nearest-neighbouring Zr of central O atoms, according to the calculated partial radial distribution function (RDF) (Extended Data Fig. 9). Subsequently, a convex hull of selected atoms can be defined by triangular tessellations and the region within the convex hull, visualized by yellow surface meshes, is referred to as Zr–O oxide network.

In addition, to characterize the topology, we calculated the fractal dimensionality of the Zr–O network in the O-containing samples by the box-counting method[39]. To avoid size effects on dimensionality in the *Y* and *Z* directions, the cell boxes were replicated to capture a large volume (19.2 × 192.0 × 192.0 nm^3) for the box-counting calculations. Extended Data Fig. 10 presents the detailed straight lines for power-law fitting.

Atomistic simulation of uniaxial compression. To understand the mechanistic origin of superelasticity, uniaxial compression parallel to the free surface was performed in the atomistic simulations. To this end, we ensure the five prepared samples for compression to be consistent in sizes (19.2 × 9.6 × 9.6 nm^3). Free surfaces were introduced in *X* direction and the periodic boundary conditions were applied in the other two directions. Strain was incrementally applied at a step of 0.1% at the temperature of 1 K and zero external pressure until the total strain reached 18.0%. The atomic structure was relaxed at each increment for a strain rate of 0.1% ps^{-1} (1 × 10^8 s^{-1}). According to the virial theorem, we obtained the engineering stress–strain curve for loading and carried out further simulations by reversing the load direction under the same conditions (for example, temperature, external pressure). For unloading, we chose six values of strain release (for example, 3%, 6%, 9%, 12%, 15% and 18%). Note that the simulations of both loading and unloading were performed on 30 replicas with the Maxwell distribution of initial momenta.

Non-affine displacement of O network. Since non-affine displacement is now routinely used to identify irreversible atom rearrangements, we considered the following temporal response of the O–O pairs as the non-affine displacement in the O network, as inspired by a seminal work[40]:

$$D^2_{\mathrm{O-O}}(t,\Delta t)=\sum_n\left|r_n(t)-(\boldsymbol{\delta}+\boldsymbol{\varepsilon})\,r_n^{\mathrm{T}}(t-\Delta t)\right|^2,$$

where $\boldsymbol{\delta}$ and $\boldsymbol{\varepsilon}$ denote the identity and strain tensors, respectively; and *n* runs over the O–O pairs within the interaction range of 4.5 Å (Extended Data Fig. 9b) from a reference O atom. According to the finite deformation theory, the solution of $\boldsymbol{\varepsilon}$ to minimize D^2 is unique. Therefore, we used the minimum value of $D^2_{\mathrm{O-O}}$ to characterize the local deviation from the affine displacement in the O network. Noted that we used the same interaction cutoff length of 4.5 Å to calculate D^2 in metals (Extended Data Fig. 8) based on the original work[40].

Data availability

The datasets used or analysed during the current study are available from the corresponding authors on reasonable request.

References

33. Wang, T. et al. The controlled large-area synthesis of two dimensional metals. *Mater. Today* **36**, 30–39 (2020).
34. Yu, Q. et al. Strong, ductile, and tough nanocrystal-assembled freestanding gold nanosheets. *Nano Lett.* **22**, 822–829 (2022).
35. Cahn, J. W. & Hilliard, J. E. Free energy of a nonuniform system. I. Interfacial free energy. *J. Chem. Phys.* **28**, 258–267 (1958).
36. Su, R. et al. Models and algorithms towards the metallic glasses vitrification at deep supercooled region. Preprint at *arXiv* https://doi.org/10.48550/arXiv.2211.03350 (2023).
37. Thompson, A. P. et al. LAMMPS—a flexible simulation tool for particle-based materials modeling at the atomic, meso, and continuum scales. *Comput. Phys. Commun.* **271**, 108171 (2022).
38. Parrinello, M. & Rahman, A. Polymorphic transitions in single crystals: a new molecular dynamics method. *J. Appl. Phys.* **52**, 7182–7190 (1981).
39. Hu, Y. C. et al. Unveiling atomic-scale features of inherent heterogeneity in metallic glass by molecular dynamics simulations. *Phys. Rev. B* **93**, 214202 (2016).
40. Falk, M. L. & Langer, J. S. Dynamics of viscoplastic deformation in amorphous solids. *Phys. Rev. E* **57**, 7192–7205 (1998).

Acknowledgements

The research of Y.Y. is supported by the research grant council (RGC), the Hong Kong government, through the general research fund (GRF) with grant nos. N_CityU 109/21, CityU11200719 and CityU11213118. P.F.G. acknowledges support from the NSF of China (grant nos. 5211101002, 12088101 and U2230402). We acknowledge computational support from the Beijing Computational Science Research Center (CSRC). Y.H.L. acknowledges support from the National Natural Science Foundation of China (grant no. 51825104). F.L. acknowledges support from the China Postdoctoral Science Foundation (grant no. 2020TQ0346); Guangdong Major Project of Basic and Applied Basic Research, China (grant no. 2019B030302010); and the National Natural Science Foundation of China (grant no. 52201195). Y.L. acknowledges support from RGC under RFS2021-1S05. J.W. acknowledges support from the NSF of China (grant no. 52071081).

Author contributions

Y.Y. supervised the project. Y.Y., Y.H.L. and P.G. conceived the idea. N.B., T.C. and J.P.C. fabricated the MG nanotubes. Z.Z. fabricated the MG nanosheets. F.L. performed the TEM characterization. F.L. and J.L. carried out the 3D-APT characterization. F.L., X.F. and H.Z. performed the in situ microcompression. Z.Z. performed the AFM characterization. H.L. performed the atomistic simulations. W.Z., Z.Z., T.W. and M.P. performed the FEM simulations. J.Z. carried out the digital image correlation analysis. F.L., H.L., Z.Z., T.W., J.W., X.L., Y.L. Y.H.L., Y.Y. and P.G. contributed to the data analyses. F.L., H.L., Z.Z., P.G. and Y.Y. wrote the manuscript.

Competing interests
The authors declare no competing interests.

Additional information
Extended data is available for this paper at https://doi.org/10.1038/s41563-023-01733-8.

Supplementary information The online version contains supplementary material available at https://doi.org/10.1038/s41563-023-01733-8.

Correspondence and requests for materials should be addressed to Yanhui Liu, Pengfei Guan or Yong Yang.

Peer review information *Nature Materials* thanks Mehdi Jafary-Zadeh, Gang Sha and Sang Ho Oh for their contribution to the peer review of this work.

https://doi.org/10.1038/s41563-023-01733-8

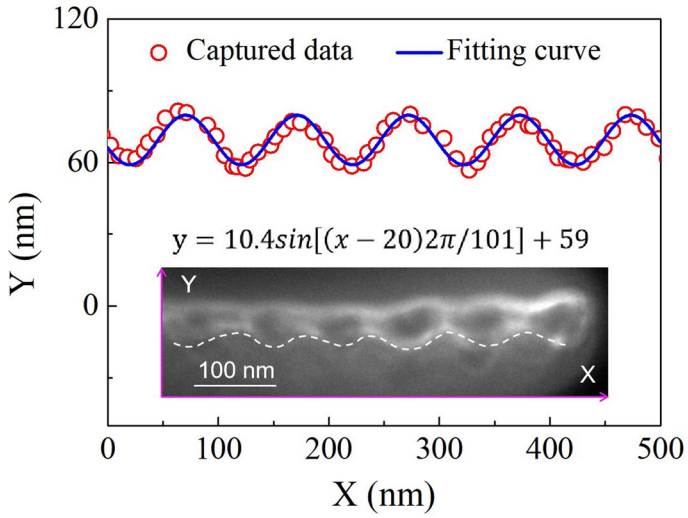

Extended Data Fig. 1 | The characterization of the wavy structure of a metallic-glass nanotube. The wave-like profile extracted from the vertical-sectional view (the inset) of a ZrCuAlNi(O) metallic-glass nanotube, which can be fitted well to a sinusoidal function.

https://doi.org/10.1038/s41563-023-01733-8

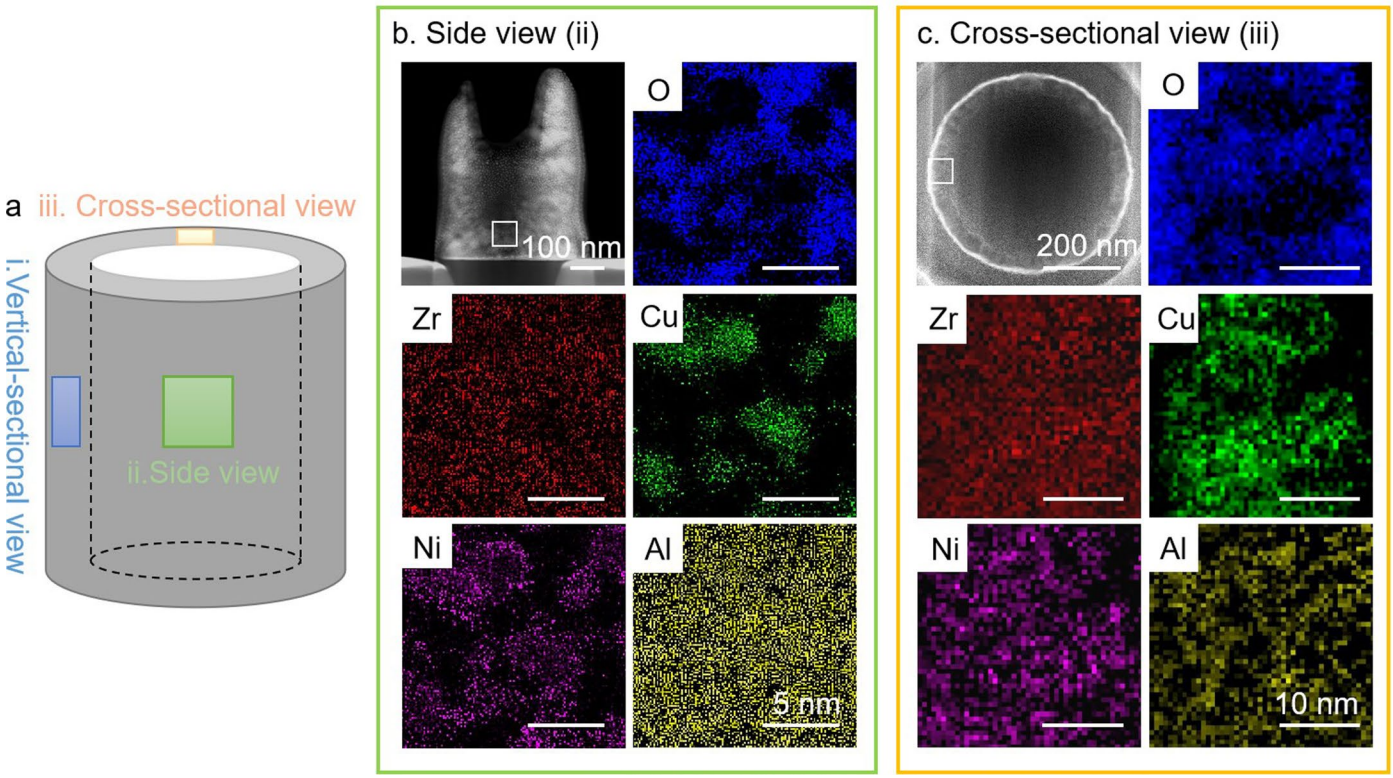

Extended Data Fig. 2 | The compositional characterization of the ZrCuAlNi metallic-glass nanotube. a. The Schematic diagram illustrating the different view directions for structural observation, **b.** EELS mapping of different elements from the side view of nanotubes, **c.** EELS mapping of different elements from the cross-sectional view of nanotubes.

https://doi.org/10.1038/s41563-023-01733-8

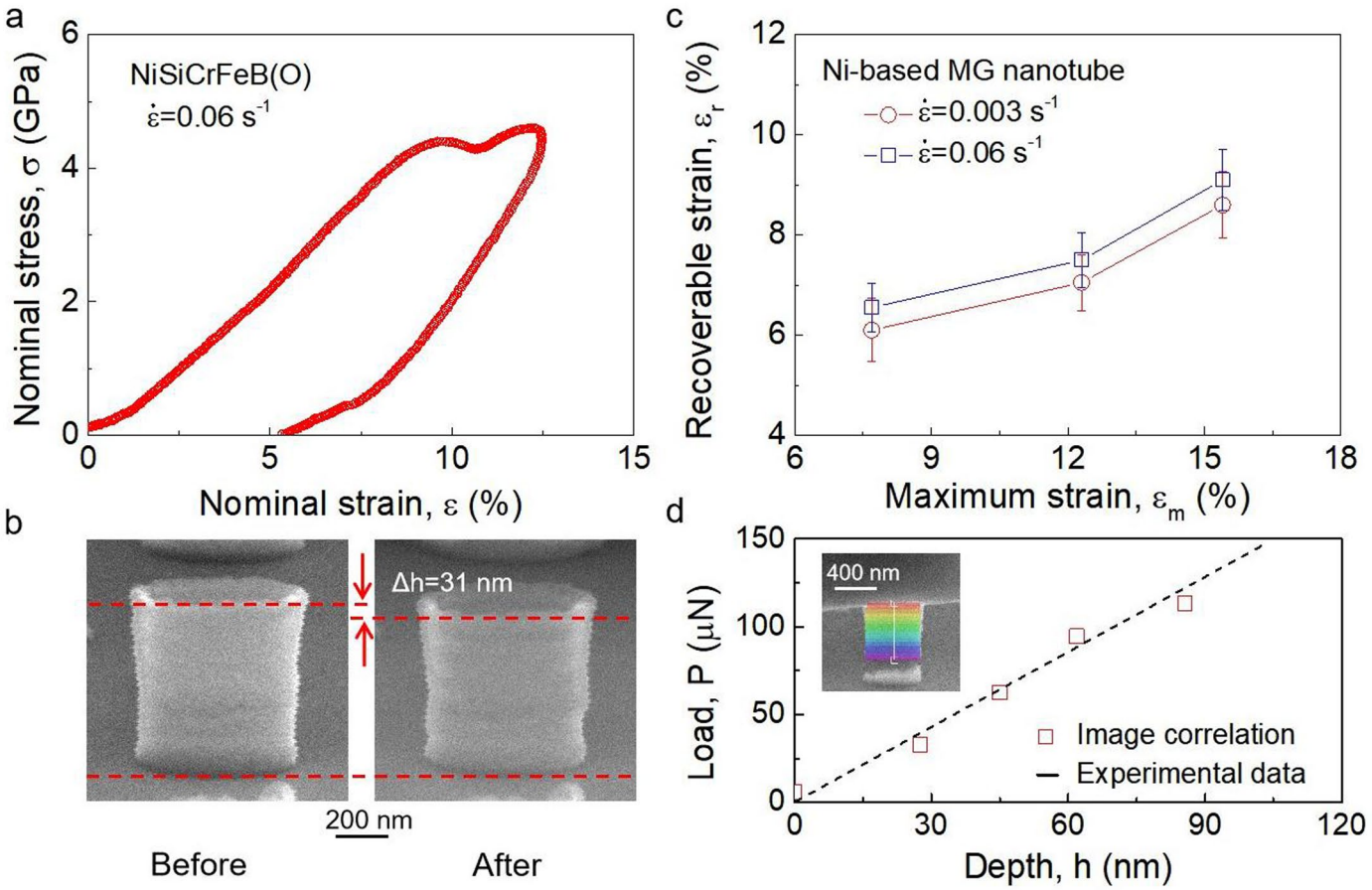

Extended Data Fig. 3 | Mechanical characterization of NiSiCrFeB(O) metallic-glass nanotubes. a. A nominal stress-strain curve of the NiSiCrFeB(O) metallic-glass nanotube under in-situ micro-compression subject to the strain rate of 0.06 S^{-1} and the maximum strain of 15.4%, **b**. The SEM images of the corresponding NiSiCrFeB(O) metallic-glass nanotube before and after microcompression, **c**. Effect of the maximum strain on the recoverable strain at the strain rate of 0.06 S^{-1} or 0.003 S^{-1}. Note that the recoverable strains measured from image correlations were repeated five times for averaging and data are presented as mean values +/−SD. **d**. Comparison of the load-depth data obtained from the indenter tip displacement and image correlation.

https://doi.org/10.1038/s41563-023-01733-8

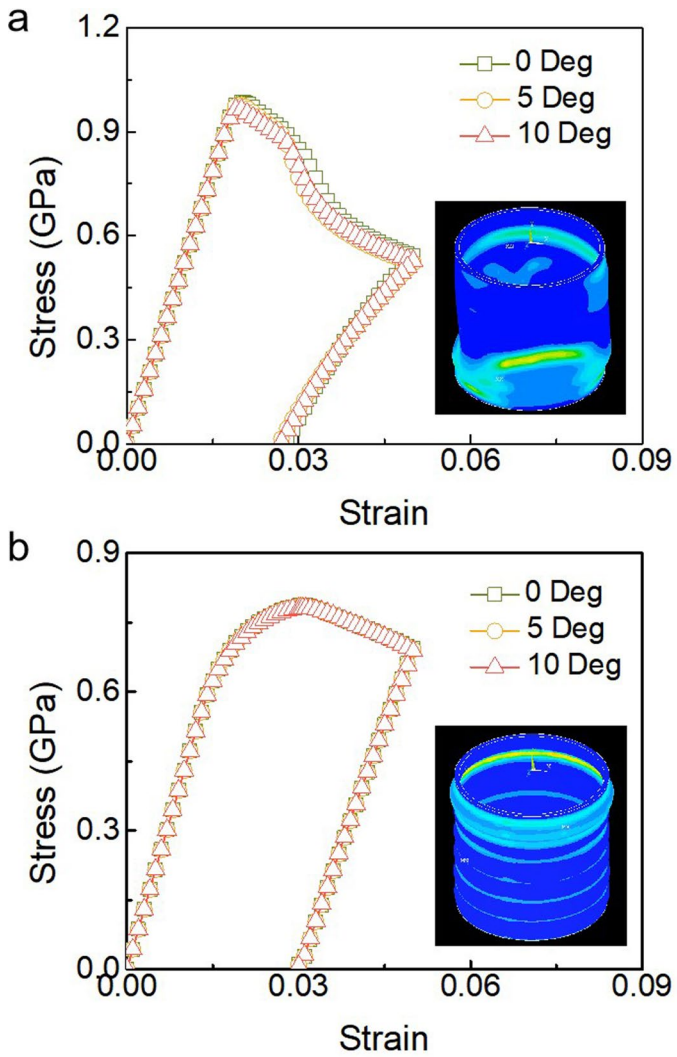

Extended Data Fig. 4 | The FE simulated mechanical behavior of wavy tubes subject to an eccentric load with varying angles of misalignment. a. The mechanical behavior of the regular tubes at the misalignment angle of 0 to 10 degrees, **b**. The mechanical behavior of the wavy tubes with a straight profile at the misalignment angle of 0 to 10 degrees. Both insets show the plastically deformed tubes that follow the conventional Drucker-Prager yield criterion.

https://doi.org/10.1038/s41563-023-01733-8

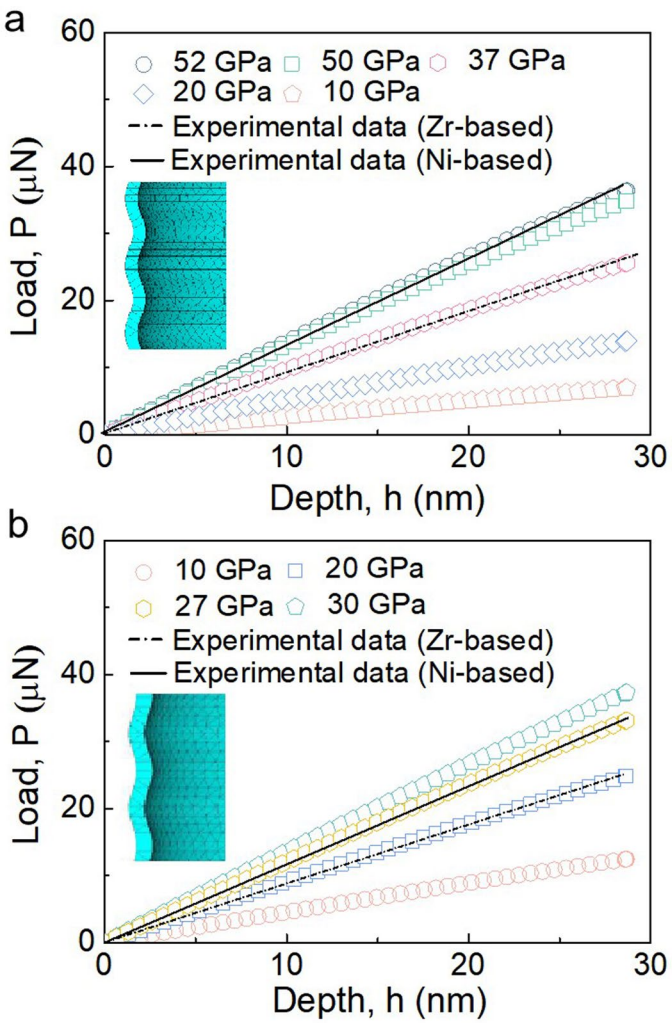

Extended Data Fig. 5 | Fitting of the experimental data to the elastic FE simulations for both ZrCuNiAl(O) and NiSiCrFeB(O) metallic-glass nanotubes. a. FEM fitting of the elastic modulus for both ZrCuNiAl(O) and NiSiCrFeB(O) metallic-glass nanotubes. The insect = the wavy profile with thickness = 15 nm, wavelength = 80 nm, and amplitude = 5 nm, **b**. FEM fitting of the elastic modulus for both ZrCuNiAl(O) and NiSiCrFeB(O) metallic-glass nanotubes. The insect = the wavy profile with thickness = 25 nm, wavelength = 105 nm, and amplitude = 10 nm.

https://doi.org/10.1038/s41563-023-01733-8

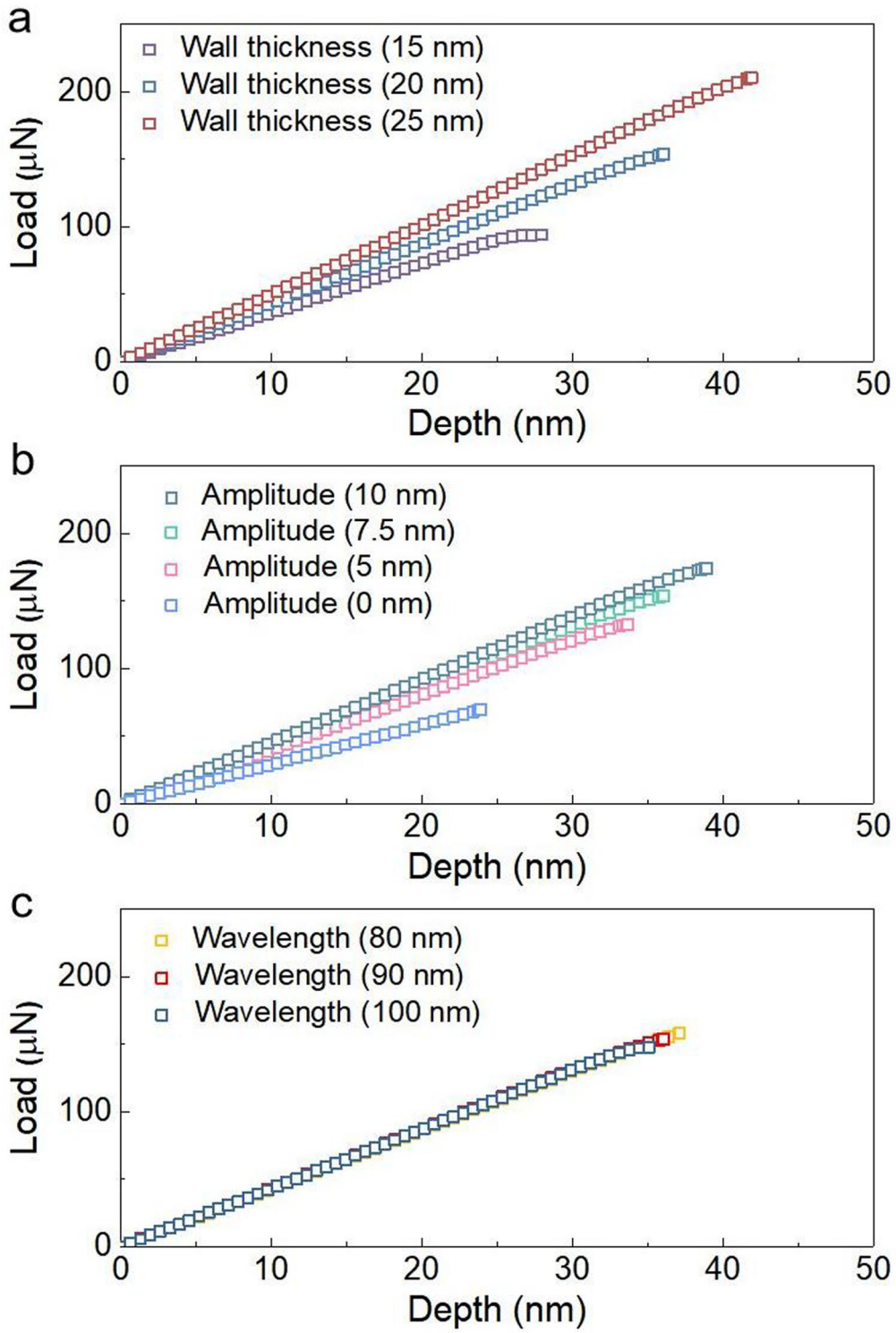

Extended Data Fig. 6 | The effects of size and geometry of tubes on their elastic responses according to our FE simulations. The effect of **a**. wall thickness, **b**. wave amplitude, and **c**. wavelength.

https://doi.org/10.1038/s41563-023-01733-8

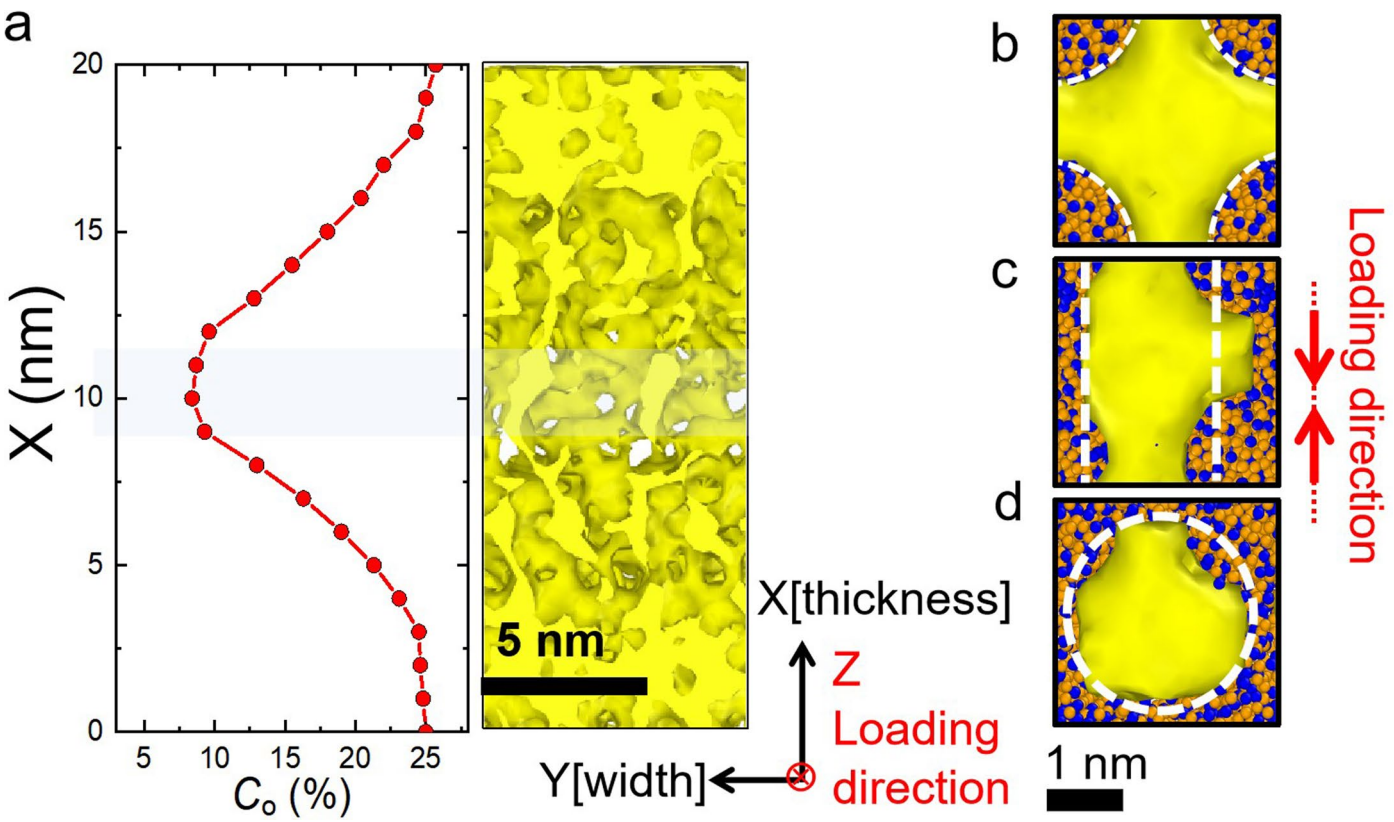

Extended Data Fig. 7 | Atomistic model of O-containing samples. Oxide network visualized by smooth surface meshes (yellow), referred to as **a**. 'O-18%'. **b**. 'model 1', **c**. 'model 2' and **d**. 'model 3' samples with an alignment to the YZ plane for the sake of compressive loading simulations.

https://doi.org/10.1038/s41563-023-01733-8

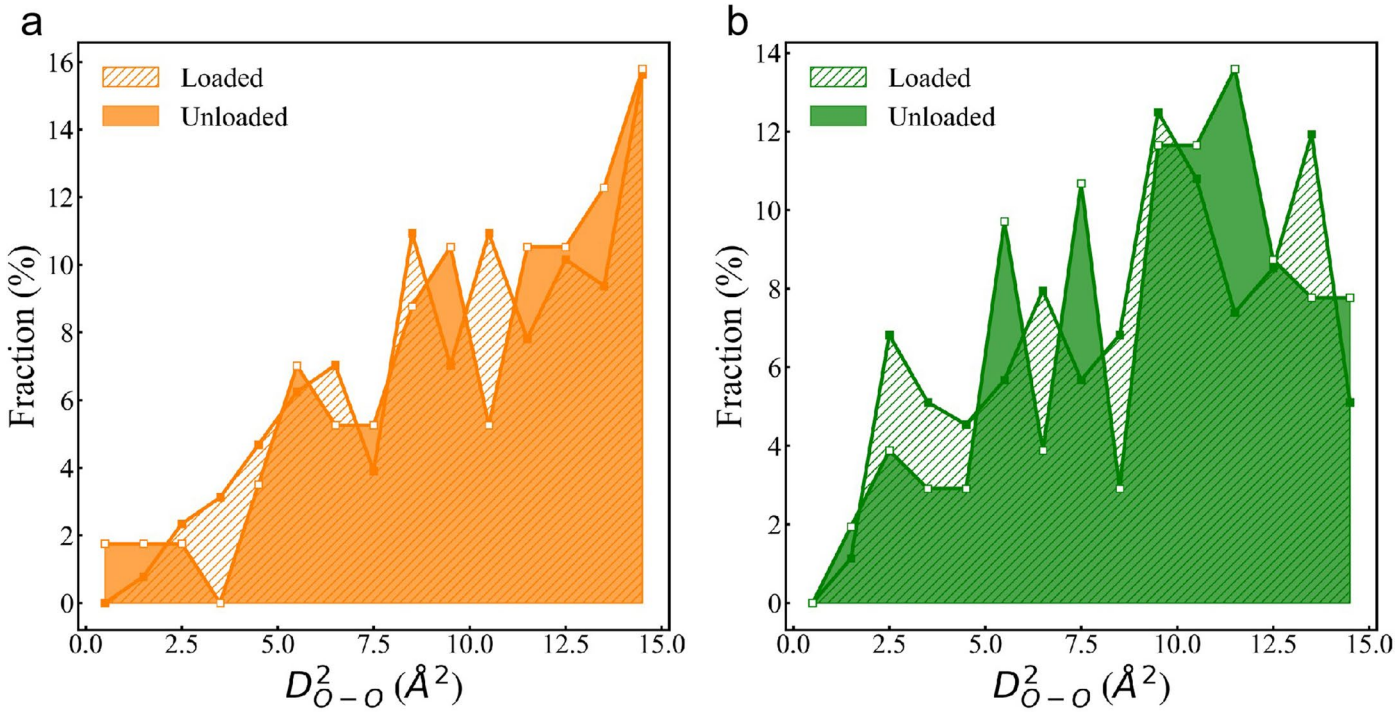

Extended Data Fig. 8 | Plastic deformation of a metallic nature in ZrCu MG domains. Distribution of D^2 in ZrCu MG domains calculated in the **a**. percolating (averaged in model 1 and 2) and **b**. non-percolating (model 3) samples.

https://doi.org/10.1038/s41563-023-01733-8

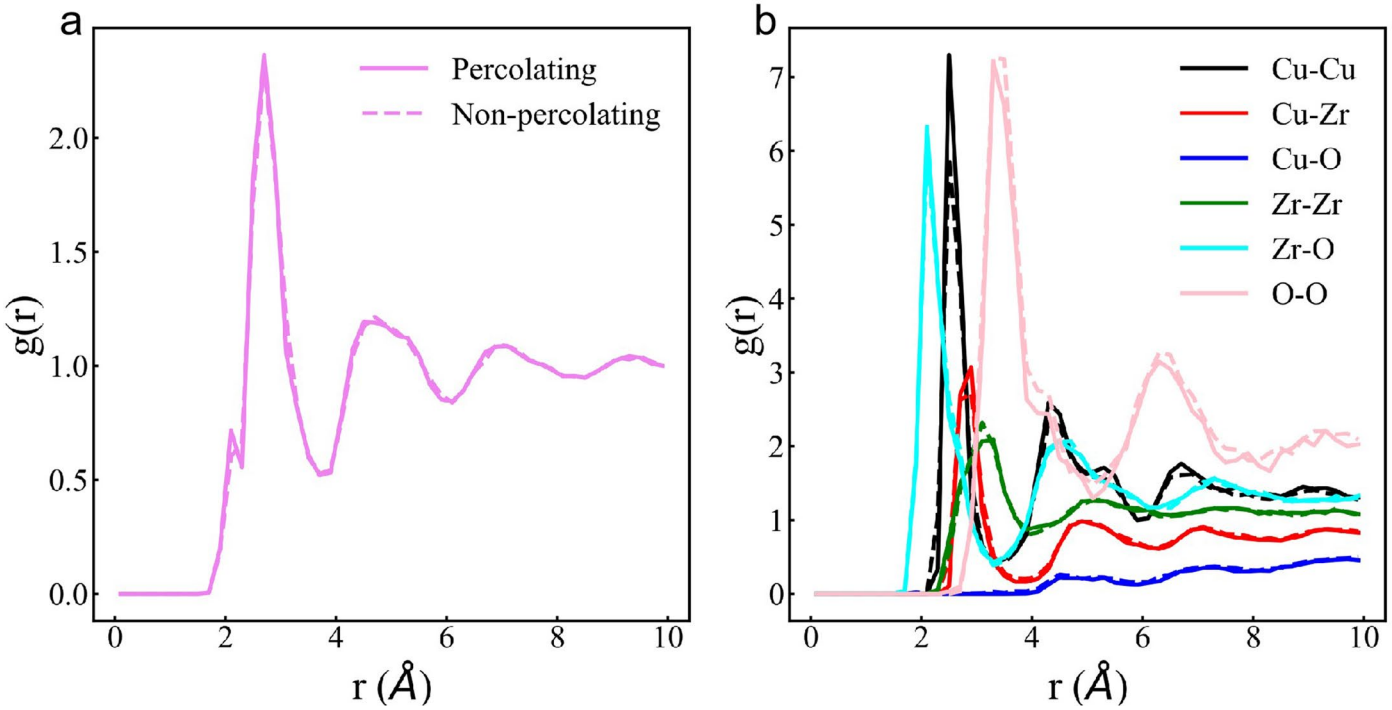

Extended Data Fig. 9 | Structural characteristics of the percolating (model 1, C_o ~ 18%, solid lines) and non-percolating (model 3, C_o ~ 17.5%, dashed lines) CuZr(O) models. a. Total pair correlation function and **b**. partial pair correlation function.

https://doi.org/10.1038/s41563-023-01733-8

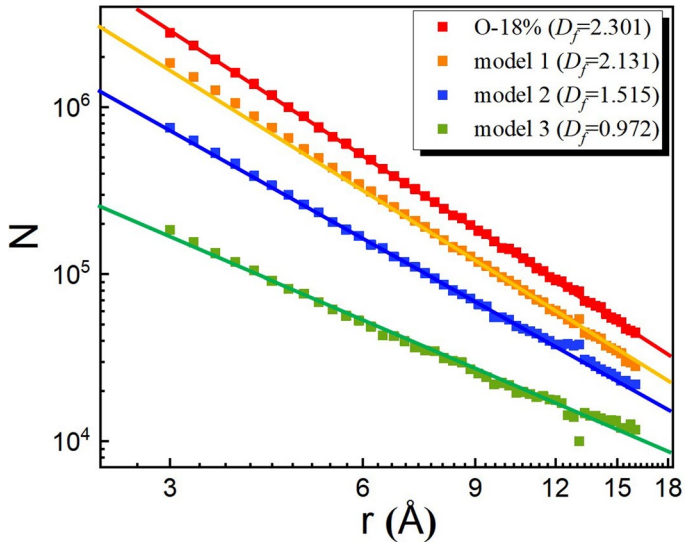

Extended Data Fig. 10 | Power law fitting of box-counting dimension. Fractal dimensionality D_f of the O-18% (red), model 1 (orange), model 2 (blue) and model 3 (green) samples computed by the counting box method. The straight lines are power fittings of box number from box size: $N \sim r^{-D_f}$.